Pseudo-prospective forecasting of induced and natural seismicity in the Hengill Geothermal field

V. A. Ritz[1], L. Mizrahi[1], V. Clasen Repollés[1], A. P. Rinaldi[1], V. Hjörleifsdóttir[2], S. Wiemer[1]

[1]Swiss Seismological Service, ETH Zürich, Zürich, Switzerland
[2]Reykjavik Energy (OR), Reykjavik, Iceland

Key Points:

- Statistical models are used in a pseudo-prospective experiment to forecast daily seismicity rates in the Hengill geothermal field.
- ETAS-type models are able to adapt quickly to sudden changes in the seismicity rate.
- The Seismogenic Index-type model outperforms ETAS-type models outside periods of high-intensity seismic activity.

Corresponding author: V. A. Ritz, vanille.ritz@sed.ethz.ch

Abstract

The Hengill geothermal field, located in southwest Iceland, is host to the Hellisheiði power plant, with its 40+ production wells and 17 reinjection wells. Located on a tectonically active area, the field experiences both natural and induced seismicity linked to the power plant operations. To better manage the risk posed by this seismicity, the development of robust and informative forecasting models is paramount. In this study, we compare the forecasting performance of a model developed for fluid-induced seismicity (the Seismogenic Index model) and a class of well-established statistical models (Epidemic-Type Aftershock Sequence). The pseudo-prospective experiment is set up with 14 months of initial calibration and daily forecasts for a year. In the timeframe of this experiment, a dense broadband network was in place in Hengill, allowing us to rely on a high quality relocated seismic catalogue. The seismicity in the area is characterised by four main clusters, associated with the two reinjection areas, one production area an area with surface geothermal manifestations but where no operations are taking place. We show that the models are generally well suited to forecast induced seismicity, despite some limitations, and that a hybrid ETAS accounting for fluid forcing has some potential in complex regions with natural and fluid-induced seismicity.

Plain Language Summary

In the southwest of Iceland, the Hengill volcanic region is the seat of a geothermal field exploited with two power plants. The power plants provide district heating and electricity to the capital region. The area continuously experiences small to moderate earthquakes, associated to the volcanic nature of the region and to the power plant operations (injection and withdrawal of fluids from the underground). To better manage the risk posed by these earthquakes, we use statistics-based computer simulations to forecast the rate of earthquakes during a year-long experiment. The simulations are trained on 14 months of data. One of the models (the Seismogenic Index) is designed to relate rate of earthquakes to the volumes of fluids injected and withdrawn; while the other relies on statistical characteristics of earthquake sequences. We show that these computer simulations are well suited to forecast earthquake rates in the Hengill geothermal field, even though they have their respective limitations. The combination of the statistical seismicity simulations with a term accounting for the volumes does show promising results in an area with complex earthquake sequences.

1 Introduction

Iceland's capital region gets most of its district heating and a third of its electricity from the exploitation of neighbouring geothermal plants (Gunnlaugsson & Ívarsson, 2010). Located 30 km east of Reykjavik, the Hengill field hosts two major power plants supplying the capital region: Hellisheiði and Nesjavellir, with installed capacities of 303 MW_e plus 133 MW_{th} and 120 MW_e plus 150 MW_{th} respectively (Hersir et al., 2009). Nesjavellir was commissioned in 1990 while Hellisheiði started production in 2006, with the subfield of Hverahlíð beginning full scale production in late 2017.

Iceland is a seismically active country, especially along the mid-Atlantic ridge that crosses through the island (Jakobsdóttir, 2008). On top of this natural seismicity, the exploitation of deep geothermal energy can cause induced seismicity (Grigoli et al., 2017). In the Hengill field, numerous episodes of seismicity have been recorded since the early 1990s with the start of instrumental catalogues in south-west Iceland (SIL network, Icelandic Met Office). Both volcano-tectonic and induced sequences illuminating the field have been mapped to shallow depth, and the discrimination between natural and induced seismicity is particularly difficult in this area.

Although relatively isolated and with a low building density, the area around the Hengill field has seen several large events in the last decades, including two likely induced events of magnitude around 4 in October 2011. The operators of the geothermal plants thus need tools to assess and mitigate the seismic risk posed by their injection and production operations. In this study, we use probabilistic models to forecast seismicity happening in the Hellisheiði field between late 2018 and early 2021.

Statistical models have shown some encouraging results to model induced seismicity (Király-Proag et al., 2016; Verdon & Budge, 2018; Mancini et al., 2021), although these models do not account for coupled processes in the subsurface. We use two different classes of statistical models developed for very different use cases: Seismogenic Index, developed for injection-induced seismicity; and Epidemic-Type Aftershock Sequence (ETAS) models that are widely used for natural seismicity modelling. The Seismogenic Index is a simple yet robust model that relies on a linear relationship between volume rate and seismicity rate, and has proven its reliability in numerous induced seismicity sequences (Mignan et al., 2021, 2017). Recent work showed that its parameters can be updated in near real time during stimulations (Broccardo et al., 2017; Mignan et al., 2019;

Broccardo et al., 2019). The Epidemic-Type Aftershock Sequence relies on several empirical observations, from the Gutenberg-Richter power law to Omori's law for aftershock decay. ETAS models are at the forefront of operational earthquake forecasting (Marzocchi et al., 2014; Nandan et al., 2021).

We try to answer a few questions: How do Seismogenic Index-type models tailored to induced seismicity compare to ETAS based models adapted from natural to mixed seismicity with fluid forcing term compare? How do these models perform in forecasting the seismicity, retrospectively? What can these models tell us about the seismicity in the Hengill geothermal field?

2 Geological context

The Hellisheiði geothermal field is located in south-west Iceland, 30 km east of Reykjavik. The field is nested between three volcanoes: Hengill to the north, Hrómundartindur to the north-east, and Grænsdalur to the east. Mount Hengill was last active around 2000 years ago, while Hrómundartindur was last active circa 10,000 years ago, and Grænsdalur has been extinct for 300,000 years (Jousset et al., 2011; Foulger & Toomey, 1989; Sánchez-Pastor et al., 2021). The area forms the junction of three tectonic systems: The Reykjanes Peninsula oblique rifting system (RP), the South Iceland Seismic Zone (SISZ) and the West Volcanic Zone (WVZ) (Tomasdóttir, 2018).

The geothermal reservoir is a water dominated fractured system, comprising basaltic lava layers, hyaloclastites series and dyke intrusions (Snaebjonsdottir et al., 2018; Franzson et al., 2005), with and average porosity of 10 % (Gunnarsson et al., 2011). Only the southern area of Hverahlíð presents a different composition with mostly lava series. The formation temperature averages between 220 and 250 °C at 1000 m b.s.l. (Gunnarsson, 2013). The produced fluid is a water-steam mix ranging in temperature between 240 and 320°C.

The area is characterised by the Hengill fissure swarm, which strikes 30 °N forming a graben structure around 40 km in length (Saemundsson, 1992). Extensional structures (normal faults) and eruptive fissures are a common occurrence (Steigerwald et al., 2020), as well as strike-slip faults oriented N-S associated with the SISZ.

The field has seen a major volcanic uplift event between 1994 and 1999, with up to 8 cm of inflation, close to 100.000 earthquakes recorded with a largest magnitude of

109 M_L 5.5 (Blanck et al., 2021; Jakobsdóttir, 2008). Two earthquakes of magnitude 6 have
110 been recorded in 2008 in the eastern part of the field, reactivating strike-slip faults (Decriem
111 et al., 2010). Following the late 1990s uplift event, subsidence has been observed since
112 the mid 2000s (Ducrocq et al., 2021), coinciding roughly with the commission of the Helli-
113 sheiði power plant in 2006.

114 2.1 Areas of interest

115 We selected four areas of seismological interest, based on the spatial clustering in
116 the COSEISMIQ catalogue. These areas are highlighted by the coloured boxes in Fig-
117 ure 1.

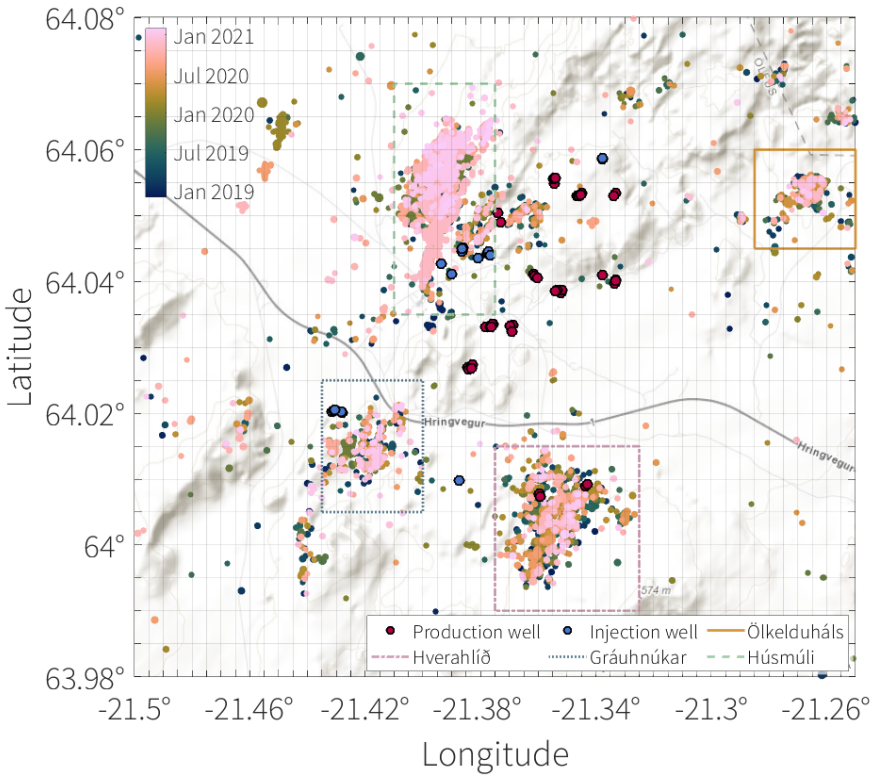

Figure 1. Distribution of injection and production wellheads in the active geothermal area. The regions highlighted by boxes are areas of specific seismological interest. The grid lines show the space discretisation for the forecasts.

2.1.1 Production areas

The Hengill field produces a water-steam mixture at an average rate of 38Mton/year (for the 2012-2015 period, Juncu et al. (2017)). The production occurs in 40+ wells located in two distinct areas: The central Hellisheiði field, and Hverahlíð, a sub-field to the south.

Hellisheiði The main production area of the Hellisheiði field has not been associated with much seismicity since the end of the volcanic event in 1999. The drilling of the production wells since 2001 in the area did not trigger seismicity (except for well HE-08). However, since 2009 and the end of drilling, there has been sustained levels of seismicity, with some seismic swarms happening intermittently (Hjörleifsdóttir et al., 2021). The area is however rather quiet during our period of interest and is thus not looked at in detail in this study.

Hverahlíð Hverahlíð is located in the south of the Hengill region and is considered a subsystem of the Hellisheiði. It hosts the most powerful wells of the Hengill field and is associated with a shallow 2-3 km deep low velocity anomaly (Sánchez-Pastor et al., 2021). The area is also characterised by a relative abundance of strike-slip faults linked to the SISZ, making the area likely even more permeable than the rest of the field (Franzson et al., 2010). The drilling of the production wells in Hverahlíð was not associated with seismicity except for well HE-21 in 2006. The production in the area started in fall 2017, coinciding with an increase in the seismicity which remains elevated as the production continues (Hjörleifsdóttir et al., 2021).

2.1.2 Reinjection areas

The reinjection of spent fluids in a geothermal field is mandated for multiple purposes: To sustain reservoir pressures, avoid subsidence and reservoir compaction, enhance the natural recharge of the system, improve thermal extractions along flow-paths, and comply with environmental regulations (Axelsson, 2012). In Hellisheiði, the reinjection occur mostly in two clusters of wells (Húsmúli and Gráuhnúkar) with a few other reinjection wells scattered within the production areas.

Gráuhnúkar Gráuhnúkar is the first dedicated reinjection of the Hellisheiði field, and is located in the south-west of the region. The six injection wells were commissioned

between 2006 and 2008, and are continuously used for reinjection purposes since then (Hardarson et al., 2010). The formation temperature is much higher than expected with temperatures reaching up to around 300 °C. The start of reinjection in Gráuhnúkar did not lead to an alarming increase in the seismicity rate, which remained low until the injection rate was increased in mid-2011. Since 2011, the seismicity has been low to moderate and seems to correlate with the injection rates and take off when the 300 L/s mark is reached (Flóvenz et al., 2015; Ritz et al., 2021).

Húsmúli The drilling of the eight wells in Húsmúli started in 2007 and continued until mid-2011. The reinjection started systematically in five of the wells in September 2011 (although some injection had been done in one of the wells since 2009; (Hardarson et al., 2010; Gunnarsson et al., 2015)). Seismicity started during the drilling operations, linked to repeated circulation losses, and remained very high during the first nine months of reinjection until the injection rates were reduced (Hardarson et al., 2010; Gunnarsson, 2013; Ágústsson et al., 2015; Kristjansdottir et al., 2021; Ritz et al., 2021). During the first year of reinjection, a 2 cm uplift was observed in Húsmúli (Juncu et al., 2018). A shallow (∼3km) deflating source has been observed in the late 2010s, potentially linked to the localised fluid extraction and circulation (Ducrocq et al., 2021).

2.1.3 Ölkelduháls area

Ölkelduháls is located to the east of our region of interest. It is characterised by surface geothermal manifestations like hot springs and fumaroles probably linked to the residual heat of Hrómundartindur volcano. A high velocity anomaly at depths 2-4 km has been identified (Jousset et al., 2010). In 1995, an exploratory well was drilled in the area, and two more have been drilled since but are not active. Ölkelduháls is very close to the center of the late 1990s volcanic uplift (estimated between 5 and 6 km depth), experienced subsidence between 2006 and 2017 and was at the center of the an inflating source mapped in 2017-2018 with up to 12 mm vertical displacement (Ducrocq et al., 2021). These deformation cycles are not well understood but have been theorised to be the results of either irregular magmatic intrusions or hydrothermal fluid migrations (or a combination of both with different layers seeing different fluids intrude or migrate). Ölkelduháls is the only region that is not highlighted because of its suspected induced seismicity, but quite some seismicity is recorded in the area

3 Data

3.1 Seismic catalogue

The seismic data was acquired as part of the COSEISMIQ project (`http://www.coseismiq.ethz.ch/en/home/`) during which the Hengill region was instrumented with a small aperture seismic array between December 2018 and February 2021. Multiple catalogues were created with different quality thresholds and relocation techniques. Here we use the high quality catalog with relative relocation (Grigoli et al., 2022). This catalogue contains about 8500 events distributed in a 35 × 30 km area centered around the Hellisheiði power plant (Figure 2).

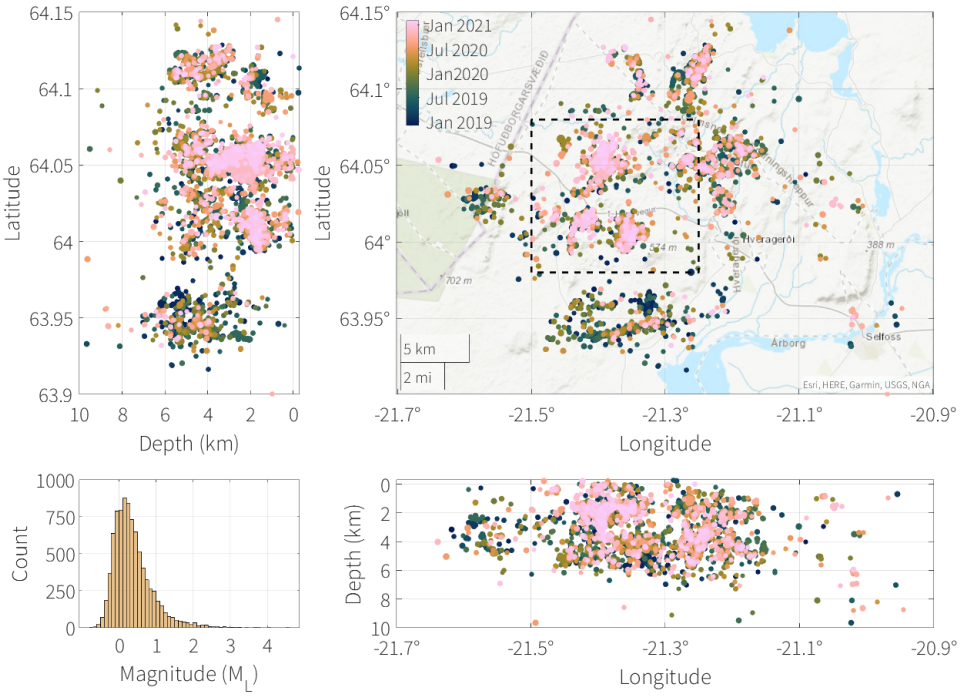

Figure 2. Distribution of seismicity in the Hengill geothermal field from 01.12.2018 to 31.01.2021, COSEISMIQ high quality hypo-DD relocated catalogue (Grigoli et al., 2022). Dot size is proportional to the magnitude, colour coded by time of occurrence. The dashed area in the main panel shows the active Hellisheiði geothermal area we focus on.

The b-value and magnitude of completeness of the catalogue are estimated jointly using a method proposed in the literature by Clauset et al. (2009); Mizrahi et al. (2021a). We assume the magnitude of completeness (M_c) to be constant both in time and space

in the area of interest and test different values of M_c, calculating for each M_c the corresponding b using the maximum likelihood approach (Marzocchi & Sandri, 2003). We then check whether the observed cumulative magnitude distribution function is plausible to be a realisation of the fitted Gutenberg-Richter (GR) law as follows. The cumulative distribution function (CDF) corresponding to the fitted discretised power law is compared to the observed cumulative distribution function using the Kolmogorov-Smirnov distance (KS-distance). The probability p_{M_c} of observing a KS-distance of at least D_{M_c} from a sample randomly drawn from a discretised GR power law is estimated through the simulation of 10,000 of such random draws. p_{M_c} is defined as the fraction of simulated samples for which the KS-distance is at least D_{M_c}. The smallest M_c for which this probability is greater than or equal to 0.1 is considered to be the magnitude of completeness of the catalogue. From this analysis we conclude that the magnitude of completeness of the catalogue is 0.3 and that the b-value is equal to 0.93 (Figure 3).

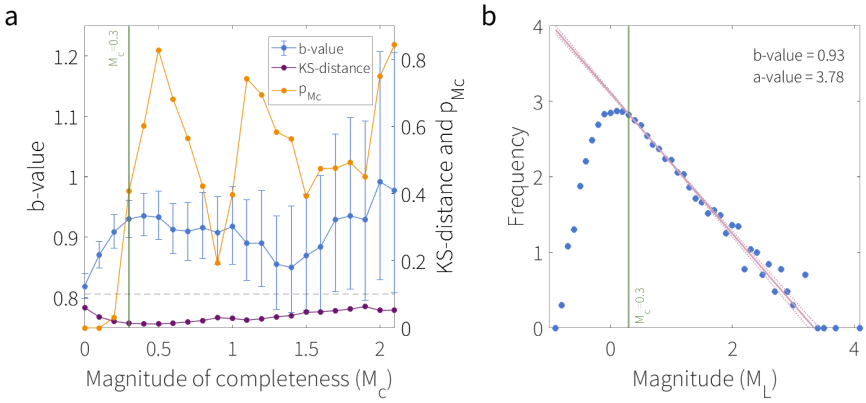

Figure 3. Statistical analysis of the catalogue

3.2 Hydraulic data

The Hellisheiði geothermal field counts 17 active reinjection wells and around 45 active production wells at all times (Figure 1). These wells are directional wells for the most part, but we only have access to the wellhead coordinates for the production wells. The wellhead coordinates are used as proxy for the feedzone locations.

Injection and production rates obtained from the power plant operator (Reykjavik Energy) are distributed in a symmetrical bi-variate Gaussian distribution around the wellhead to account for fluid migration in the subsurface with daily granularity.

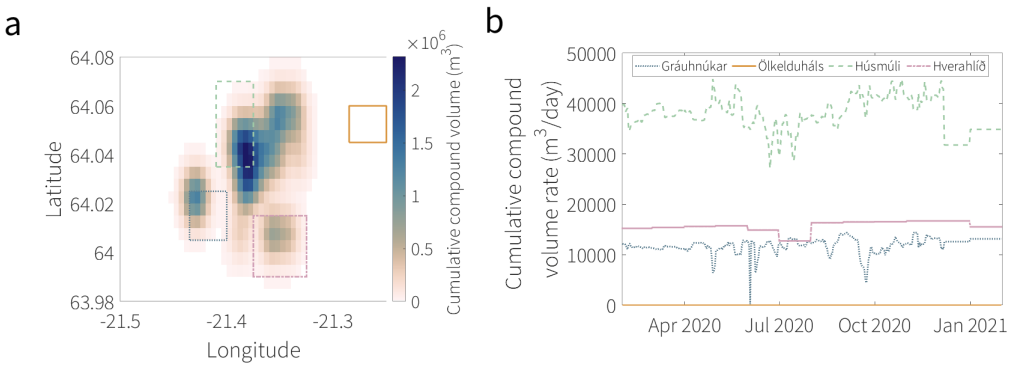

Figure 4. a) Distribution of cumulative compound volumes at the end of the experiment. b) Temporal evolution of the compound volume in the areas of interest.

It is worth noting that this isotropic distribution of the volumes is only a coarse proxy and doesn't exactly match with the areas of seismological interest (Figure 4). In particular, the volumes distributed in Gráuhnúkar are offset to the north-west compared to the seismic cluster. The wells in Gráuhnúkar actually strike south-east, and line up pretty well with the seismicity cluster highlighted by the box in Figure 4 (Hjörleifsdóttir et al., 2021; Ritz et al., 2021).

4 Models

Two families of models are implemented: a Seismogenic Index type and a class of Epidemic-Type Aftershock Sequence models.

4.1 SI - Seismogenic index model

This model is based on a purely empirical relationship between the injected volume and the seismicity, and contains a set of parameters describing the geological and seismological characteristics of the targeted site. Various versions exist in the literature after the pioneering work of S. Shapiro's group (Shapiro, 2018). Other forms account, for example, for the injection rate rather than the injected volume, as well as for an exponential decay of the seismicity after shut-in (Mignan et al., 2017; Broccardo et al., 2017). The proposed model follows the approach by Broccardo et al. (2017), providing a deterministic forecast. The expected number of events $N_{expected}$ follow the relationship:

$$N_{expected,m\geq M_c} = V_{inj/prod} 10^{a_{fb}-bM_c} \quad (1)$$

where $V_{inj/prod}$ is the compound injected and produced volume, a_{fb} the activation feedback (in m^{-3}), and b the b-value of the Gutenberg-Richter power law. This underground activation feedback a_{fb} is the a-value of the Gutenberg-Richter power law normalised by the injected volume such that $a_{fb} = a - log_{10}(V)$, and is also know as the seismogenic index in the poroelastic context (often noted Σ; Shapiro et al. (2010); Dinske and Shapiro (2013)). This parameter has also been interpreted as resulting from geometric operations on a static stress field produced by a change in the volume in the underground (Mignan, 2016). For simplicity, we refer to the model as the 'Seismogenic Index' and the productivity parameter a_{fb} as the activation feedback, and do not assign any specific physical meaning beyond that of fluid-earthquake productivity factor.

Equation 1 can be translated into an equation to determine the seismicity rate for active phases as:

$$\lambda(t, m > M_c) = \dot{V}(t) \cdot 10^{a_{fb} - bM_c} \tag{2}$$

In this model, the linear relationship between $\dot{V}(t)$ and $\lambda(t, m > M_c)$ derives from the linear relationship between injection rate and overpressure, and neglects potential temporal changes in injectivity (Mignan, 2016). Note that this equation has been extensively tested on injection-induced sequences, but not on the production phase (Broccardo et al., 2019; Mignan et al., 2017), although the classical Seismogenic Index approach is has been extended to production cases (Shapiro, 2018).

We do not account for post-injection phases and the associated seismicity decay - as modelled by Mignan et al. (2017) - as the Hengill field is in constant operation, both for production and injection.

4.1.1 Parameter estimation

For the estimation of the parameters of the Seismogenic Index model, M_c is taken from the catalogue, while a_{fb} and b are optimised for each cell by minimising the log-likelihood function (Equation 3). The Maximum Likelihood Estimate is modified from Broccardo et al. (2017) to only account for active injection and/or production phases.

$$ln\mathcal{L}(\mathcal{D}|\theta) = \frac{N(a_{fb} - bM_c)}{log(e)} + \sum_{n=1}^{N} ln(\dot{V}(t_n)) - V(t) \cdot 10^{a_{fb}-bM_c} + N \cdot ln(b) + N \cdot ln(ln(10)) - b \cdot ln(10) \cdot \sum_{n=1}^{N} m_n - N \cdot ln(10^{-bM_c} - 10^{-bM_{max}}) \quad (3)$$

This data-driven cell by cell approach allows the model to assume that the underground feedback parameter a_{fb} varies spatially within the area of interest. Supplementary Figure S1 gives an impression of the ability of the model to fit to the data by showing the difference between the recorded and expected events during the learning period. The Seismogenic Index model fits very well in the Húsmúli, Hellisheiði, and Hverahlíð regions, where there are both volumes injected and/or produced and seismic events. The model is not able to fit anything in Ölkelduháls as there are no injection or production activities. The fit in Gráuhnúkar is good in the eastern part where the volumes are present, but unsatisfactory to the west where there are no volumes distributed.

In this current state, the Seismogenic Index model is deterministic by nature and carries the assumption that induced seismicity can be described as a Poissonian process. From the optimised parameters, we calculate the mean rate of seismicity in the cell at this given time and extrapolate a poissonian distribution from it to be able to make a probabilistic comparison of the forecast to the recorded seismicity.

4.2 ETAS - Epidemic-Type Aftershock Sequence models

ETAS models (Ogata, 1988) view seismicity as a combination of background and triggered earthquakes. Background earthquakes result from tectonic forces or anthropogenic factors such as fluid injection and/or production. These background earthquakes can trigger a cohort of aftershocks which can then trigger their own aftershocks and so forth. In its simplest from the ETAS model describes the conditional seismicity rate of magnitude m events, $\lambda(t, x, y, m|\mathcal{H}_t)$, at any location (x, y) and time t as

$$\lambda(t, x, y, M|\mathcal{H}_t) = [\mu + \sum_{i:t_i<t} g(m_i, t - t_i, x - x_i, y - y_i)] \cdot \beta e^{-\beta(m-M_c)} \quad (4)$$

where μ is the background intensity function, which may or may not depend on space or time, $\mathcal{H}_t$ is the history of the process up to time t, and $g(m, \Delta t, \Delta x, \Delta y)$ describes the rate of aftershocks triggered by an event of magnitude m, at a time delay of Δt and a spatial distance $(\Delta x, \Delta y)$ from the triggering event, defined as:

$$g(m, \Delta t, \Delta x, \Delta y) = \frac{k_0 \cdot e^{a(m-M_c)} \cdot e^{-\Delta t/\tau}}{\left((\Delta x^2 + \Delta y^2) + d \cdot e^{\gamma(m-M_c)}\right)^{1+\rho} \cdot (\Delta t + c)^{1+\omega}}, \tag{5}$$

see Nandan et al. (2021) and Mizrahi et al. (2021b).

This kernel combines the fertility law which describes the number of events directly triggered by an event of magnitude m_i as $k_0 e^{a(m_i - M_c)}$, the time-based kernel containing the exponentially tapered Omori-Utsu law for aftershock decay, and an isotropic power-law spatial kernel. Note that it is implicitly assumed that the completeness magnitude M_c coincides with the magnitude of the smallest event which is capable of triggering other events.

4.2.1 Calibration of parameters

To calibrate the parameters of the ETAS model, we apply the Expectation-Maximisation algorithm (Veen & Schoenberg, 2008). In this iterative algorithm, one starts with a random initial guess for each of the parameters that need to be calibrated. The expectation step and the maximisation step are repeated, updating the current estimation of the parameters, until the difference between the parameters of two iterations falls below a desired threshold. In the expectation step, the probabilities p_{ij} that event e_j was triggered by event e_i, the probability p_j^{ind} that event e_j is independent, the expected number of background events $\hat{n}$, and the expected number of directly triggered aftershocks $\hat{l}_i$ of each event e_i, given the ETAS parameters of the current iteration, are estimated as

$$p_{ij} = \frac{g_{ij}}{\mu + \sum_{k:t_k<t_j} g_{kj}}, \tag{6}$$

$$p_j^{ind} = \frac{\mu}{\mu + \sum_{k:t_k<t_j} g_{kj}}, \tag{7}$$

and

$$\hat{n} = \sum_j p_j^{ind}, \tag{8}$$

$$\hat{l}_i = \sum_j p_{ij}. \tag{9}$$

Here, $g_{kj} = g(m_k, t_j - t_k, x_j - x_k, y_j - y_k)$ is the rate of aftershocks of event e_k at the location and time of event e_j. With these definitions, the independence and triggering probabilities are proportional to the contribution of background and aftershock triggering terms at any given time and location.

In the Maximisation step, the ETAS parameters are optimised to maximise the complete data log-likelihood, and these optimised parameters are used in the next iteration of the Expectation step.

4.2.2 Issuing a forecast through simulations

Once the ETAS parameters are calibrated based on the training catalogue, a forecast is issued by simulating 100,000 possible continuations of this training catalogue. This includes the simulation of aftershock cascades of the events in the training catalogue, and the simulation of background earthquakes which fall into the forecasting period plus their cascades of aftershocks. A detailed description of the simulation algorithm is given in Mizrahi et al. (2021a). Training as well as simulation are done for the full region of the catalogue, although they are evaluated only in the active geothermal area (Figure 2). This ensures that aftershock triggering which goes beyond the borders of the relatively small active area is still captured by the model.

Based on the simulated catalogues, the likelihood $p(k)$ of k events to occur in a spatial cell of interest during the forecasting period is then given through the empirical distribution as

$$p(k) = \begin{cases} \frac{n(k)}{100{,}000+1} & \text{if } n(k) > 0 \\ \frac{1}{m_0 \cdot (100{,}000+1)} & \text{if } n(k) = 0 \text{ and } k \leq 100 \\ 0 & \text{otherwise,} \end{cases} \tag{10}$$

where $n(k)$ is the number of simulations for which k events are observed, m_0 is the number of values k between zero and 100 for which $n(k) = 0$. To avoid zero probabilities for values of k that do not appear in the simulations, i.e. $n(k) = 0$, this definition of $p(k)$ includes a water-level probability for all $k \leq 100$.

4.2.3 ETAS variants

The four ETAS variants applied in this study differ only in their formulation of the background seismicity term.

4.2.3.1 ETAS-0 In the most basic variant, ETAS-0, μ is considered constant in space and time during parameter calibration. This means that the background term which determines independence and triggering probabilities in Equations (6-7) is the same for all events, irrelevant of where and when they take place.

For the simulation of catalogue continuations, the background seismicity term is space-dependent. While the number of simulated background earthquakes during the forecasting period is simulated from the constant parameter μ, their locations are simulated by randomly drawing locations of earthquakes in the training catalogue, weighted by their probability of being a background event, and adding a distortion drawn from a Gaussian distribution with mean 0 and $\sigma = 0.5$ km.

4.2.3.2 Varying background rate The second ETAS variant considered in this study uses a space-varying background term $\mu(x, y)$ during model calibration. In each iteration of the Expectation-Maximisation algorithm, $\mu(x, y)$ is calculated as

$$\mu(x, y) = \frac{1}{T} \cdot \sum_j p_j^{ind} \cdot k(\Delta x_j, \Delta y_j), \tag{11}$$

where $k(\Delta x_j, \Delta y_j)$ is a Gaussian kernel with bandwidth $\sigma = 0.5$ km applied to the distance $(\Delta x_j, \Delta y_j)$ of event e_j to the location (x, y), and T is the time length of the training catalogue. This model corresponds to the flexible ETAS model with free background described by Mizrahi et al. (2023).

4.2.3.3 ETAS with fluid forcing ETAS-type models have been used in induced seismicity contexts (Bourne & Oates, 2017; Mena et al., 2013), generally in regions with low natural background seismicity where the calibration could focus on induced earthquakes only. However, fluid-driven seismicity has distinct spatio-temporal characteristics from tectonic-loading driven seismicity and requires its own parameters when we want to model complex areas with both induced and natural seismicity.

For single-well injections, Bachmann et al. (2011) introduced an external forcing on the background rate linearly proportional to the injection rate, and found this model to perform better than the standard ETAS in a pseudo-forecasting experiment of the hydraulic stimulation in Basel (Switzerland). More recently, the same approach has been applied to a hydraulic fracturing context with promising results (Mancini et al., 2021).

We here introduce an ETAS variant ETAS-f with the background term

$$\mu(x, y, t) = \mu_{tect} + \iota \cdot V(x, y, t), \tag{12}$$

which, in addition to the tectonic background rate μ_{tect}, comprises a fluid background rate $\mu_{fluid} = \iota \cdot V(x, y, t)$ which is proportional to the compound volume (sum of produced and injected volumes) $V(x, y, t)$. The independence (or background) probability p_j^{ind} defined in Equation (7) can be split into a tectonic and a fluid part

$$p_j^{tect} = \frac{\mu_{tect}}{\mu(x, y, t) + \sum_{k:t_k<t_j} g_{kj}}, \tag{13}$$

$$p_j^{fluid} = \frac{\mu_{fluid}}{\mu(x, y, t) + \sum_{k:t_k<t_j} g_{kj}}, \tag{14}$$

and analogously the expected number of background events is the sum of the expected number of tectonically triggered and fluid triggered background events, $\hat{n}_{tect}$ and $\hat{n}_{fluid}$. The new parameter $\iota[\frac{\text{events}}{m^3}]$ can be calibrated in the Maximisation step of the expectation-maximisation algorithm as

$$\hat{\iota} = \frac{\hat{n}_{fluid}}{\iiint_{\mathcal{R},\mathcal{T}} V(x, y, t)\, dx\, dy\, dt}. \tag{15}$$

When a forecast is issued for this ETAS-f model, two types of background earthquakes are simulated, tectonic and fluid-induced ones. Both types of background events can trigger cascades of aftershocks. The number of induced earthquakes simulated in a given cell on a given day is determined by the compound volume of that cell on that day. Note that this is based on the assumption that the planned compound volume for that day is already known at the time the forecast is issued, which is a reasonable assumption for short enough forecasting horizons and in a geothermal field with stable exploitation conditions like Hellisheiði. The locations of simulated induced earthquakes within a cell are generated using a uniform spatial distribution inside the cell for which the volume is given.

This modification of the ETAS model can be applied to the standard ETAS version as well as the version with spatially varying (tectonic) background seismicity. This yields a total of four variants of ETAS: ETAS-0, ETAS with varying background, ETAS-f, and ETAS-f with varying background.

Note that this formulation of ETAS with fluid forcing is based on several simplifying assumptions. No difference is made between injected and produced volume, the effect of fluids on seismicity is assumed to be immediate and only valid on the current forecasting horizon, induced seismicity is assumed to be proportional to compound volume, etc. If this simple approach produces promising results, these assumptions can be revisited in future studies and a more realistic formulation of the fluid-induced term can be applied. In particular, production and injection could be split into two terms to better account for the differences in physics behind the triggering of induced events in the different settings.

4.3 Model comparison framework

Evaluating the performance of a model to reproduce or forecast induced seismicity is not an easy task, but is a necessary step to the implementation of ensemble modelling with model-specific weights (Király-Proag et al., 2018). Different classes of models have intrinsic assumptions that make it difficult to do direct comparison, in particular in the statistical or stochastic expression embedded in the models. Guidelines have been proposed to standardise the evaluation of models, in particular the 'Induced Seismicity Testbench' (Király-Proag et al., 2016), and the guidelines developed by the Collaboratory for the Study of Earthquake Predictability (CSEP, `https://cseptesting.org/`).

Each model provides a forecast consisting of a probability distribution of the number of earthquakes for each time and spatial bin. To evaluate and rank model performance, we use a probabilistic score: The log-likelihood, which is the natural logarithm of the probability of the model matching the recorded number of events in the time and space bin. For each time bin, the log-likelihood is summed up over the spatial cells to obtain the 'score' of the model at this forecasting horizon. The log-likelihood is then accumulated over time into the cumulative spatial joint log-likelihood to show the evolution of the forecasting performance and compare models.

We use the Information Gain to measure the predictive performance of a model compared to that of a reference model (Kagan & Knopoff, 1987). In this study, the standard version of ETAS is used as the reference model. The Information Gain is calculated as the difference of the log-likelihoods of the models, and is positive when the model performs better than the reference model and vice-versa.

ETAS models provide a full probability distribution of the expected event number per spatial cell as described in Equation (10). In the case of the Seismogenic Index, we assume a Poissonian distribution with the forecast number of event as the mean λ of the distribution.

4.4 Forecasting framework

The pseudo-prospective forecasting experiment runs between December 2018 and the end of January 2021, the period being covered by the COSEISMIQ high-quality relocated catalogue. The first 14 months are used as a learning period to train the models (1.12.20218 - 31.1.2020). We then perform daily forecasts for 365 days (1.2.2020 - 31.1.2021). After each forecasting horizon, the day is added to the calibration data-set (Figure 5).

The area of interest is centered around the production region of Hellisheiði and encompasses the reinjections regions of Húsmúli and Gráuhnúkar, as well as the production sub-field of Hverahlíð. We discretise the space in 0.005 °latitude × 0.005 °longitude spatial bins. The forecasts are issued for each spatial and temporal bins.

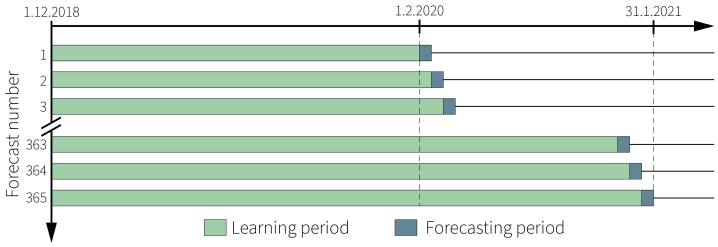

Figure 5. Schematic illustration of the pseudo-forecasting experiments

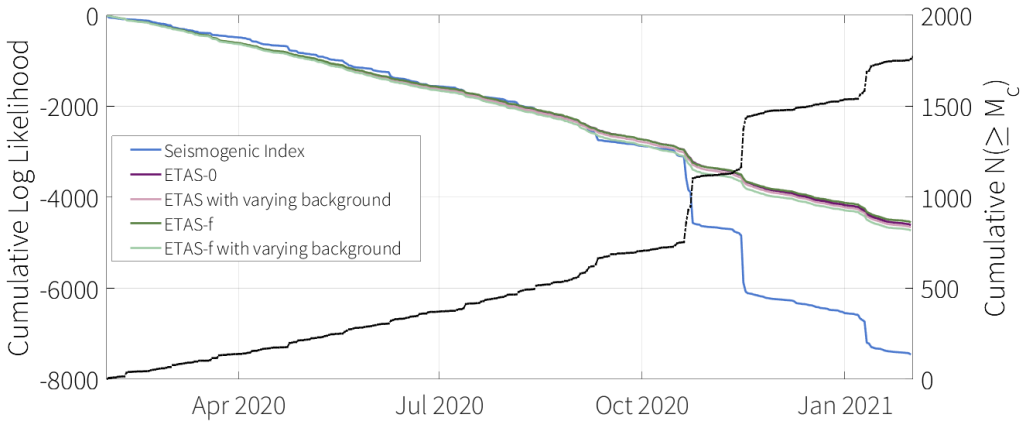

Figure 6. Cumulative spatial joint log-likelihood and cumulative number of recorded events above completeness in the active region.

5 Results & Discussion

5.1 General performance of the models

We evaluate the absolute and relative predictive performance of the models over a one year period. Figure 6 shows the cumulative spatial log-likelihood in time for each model for the active region. This metric evaluates the consistency of the models with the observations, with a log-likelihood closer to zero indicating a better model performance. All models exhibit a somehow jagged behaviour during periods of higher seismic intensity, which is expected. All models typically give higher likelihood to small event numbers than large event numbers, and thus periods with high seismicity rates will generally have more negative log-likelihoods than quiet periods. The Seismogenic Index is quite competitive with the ETAS models until October 2020, when it plunges down and is unable to explain a sudden increase in seismicity, that the ETAS models manage to accommodate. The cumulative number of events presented in Figure 6 only shows the events recorded during the forecasting period, to account for all the recorded seismicity, and does not include the 1093 events above completeness recorded during the learning period.

In Figure 7, we compare the different ETAS variants and the Seismogenic Index to a reference model, by visualising their cumulative information gain over time with respect to the standard version ETAS-0. It is worth noting that the vertical scale of the

figure is cut-off at -600, but that the Seismogenic Index's information gain plunges all the way down to -2900 by the end of the forecasting period. The Seismogenic Index performs quite well in the beginning, outperforming all ETAS models. Its downfall comes in October 2020, as the first high-intensity period takes place with sudden high rates of seismicity that the model cannot accommodate. The version of ETAS with fluid forcing outperforms the standard ETAS model by the end of the forecasting experiment, showing that in a geothermal area with active injection and production, accounting for the volumes does improve the forecasts. However, the gain is limited for most of the study period until October 2020 which sees a shift in the baseline seismicity rate with heightened activity in the reinjection area of Húsmúli. On the other hand, the varying background versions of ETAS don't perform as well as the standard version of ETAS. Possibly, the formulation of the varying background seismicity used here is not well-suited to describe a complex field like the present one. Giving too much flexibility to the background part of seismicity can make the model wrongly interpret local phenomena or fluid-induced seismicity as variations in background seismicity rate. In future studies, the bandwidth σ determining the spatial smoothing in Equation (11) could be calibrated as a hyperparameter, or a different type of smoothing could be tested to obtain better performance.

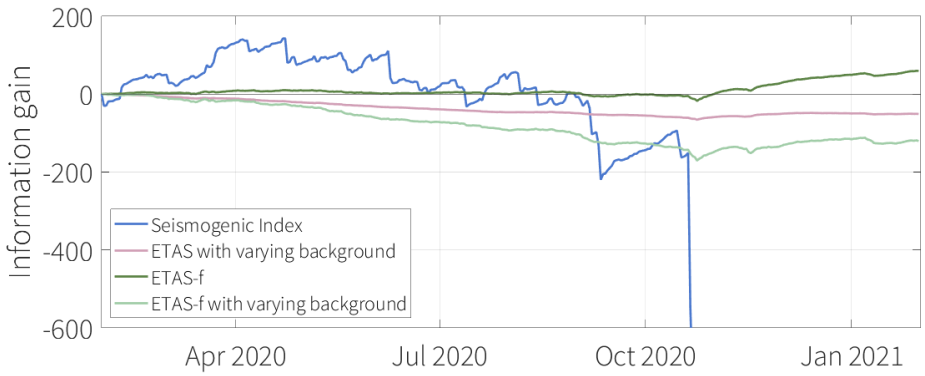

Figure 7. Cumulative information gain of ETAS and Seismogenic Index models calculated relative to ETAS-0. The vertical scale is cut-off at -600, but the Seismogenic Index pluges all the way down to -2900 by the end of the forecasting period.

5.2 How do models perform in the subregions of interest?

We evaluate the models in four separate subregions of specific seismological interest by summing the log-likelihoods within the boundaries of each region.

Ölkelduháls is not a region with active injection or production so the Seismogenic Index Model does not give any forecast for the region (Figure 8 top right panel). 73 events were recorded during the learning period, and 69 events are recorded during the forecasting period. In this subregion, the standard ETAS yields the most performant forecast, closely followed by ETAS with varying background rate (Figure 9 top right panel). It it not surprising that the versions of ETAS-f under-perform in this subregion as there should be no influence of the fluids. This also further supports the idea that the bad overall performance of ETAS with varying background is due to the model interpreting the influence of fluid injection and/or production as variations in the background.

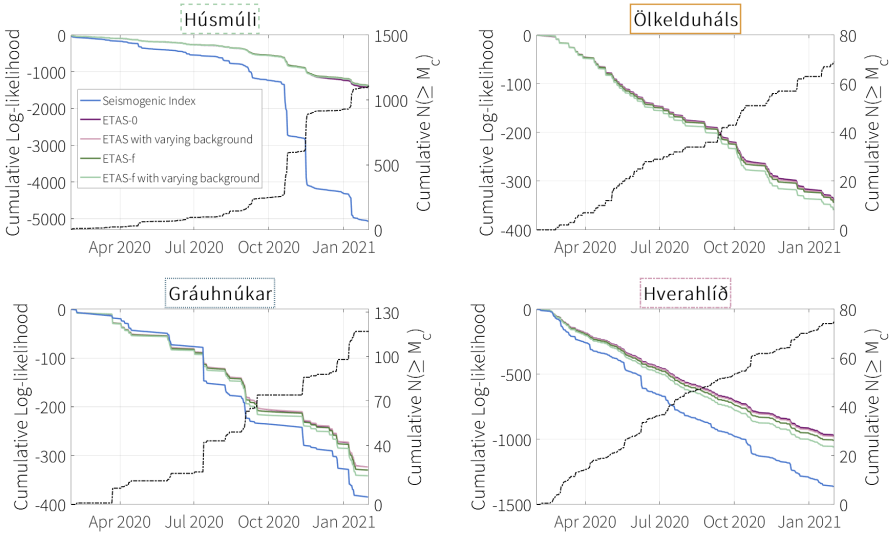

Figure 8. Cumulative log-likelihood and cumulative number of recorded events above completeness by subregion.

Hverahlíð sees a similar pattern, with standard ETAS remaining the most well-suited model (Figure 8 bottom right panel). The area is relatively seismically active with 224 events recorded during the learning period, and 282 events are recorded during the forecasting period. The poorer performance of ETAS-f models in the subregion suggests that for production areas, the cumulative extracted volume is not a good proxy for the seis-

456 micity rate. Induced earthquakes in production areas (for oil and gas or geothermal en-
457 ergy) are often a response to reservoir compaction caused by long-term production. Hver-
458 ahlíð has been in full operation since in late 2017, so these long-term effects are unlikely
459 to be already visible. The area was also not associated with particular vertical displace-
460 ment in an geodetic data and InSAR between 2015 and 2018 by Ducrocq et al. (2021).
461 In the future, we will investigate other metrics to account for fluid production, for ex-
462 ample including a proxy term for poroelasticity and/or pore-pressure instead of a cou-
463 pling with produced volumes per day.

464 In the reinjection areas, the results are more contrasted. Gráuhnúkar only sees mod-
465 erate seismicity at rather smooth rates (Figure 8); 99 events were recorded during the
466 learning period, and 117 events are recorded during the forecasting period. The evolu-
467 tion of the relative performance of the Seismogenic Index is quite interesting, as it out-
468 performs all models for the first half of the forecasting period, before taking a dive in
469 July 2020 when an increase in the seismicity rate in the region happens (Figure 9). In
470 the Gráuhnúkar area, ETAS-0 and ETAS with varying background perform better than
471 the versions with fluid forcing despite the injections being significant with roughly 12,000
472 m^3/day injected (Figure 4). The seismicity is known to be associated with the injections
473 as the area was quiet beforehand (Flóvenz et al., 2015; Ritz et al., 2021). We would ex-
474 pect that ETAS-f picks up the injection-induced characteristics, however, the injections
475 have been sustained since 2006 at very similar rates, which could explain how ETAS in-
476 terprets the low-level seismicity as background, as our learning period doesn't cover pre-
477 injection periods.

478 Húsmúli on the other hand, is the main seat of seismicity in the whole region; 579
479 events were recorded during the learning period, and 1110 events are recorded during
480 the forecasting period (8 top left panel). The reinjection in Húsmúli is mixed with pro-
481 duction at the eastern border of the area, with compound volumes varying between 30,000
482 and 40,000 m^3/day (Figure 4). The area is known for its reactivity to injection changes
483 (Gunnarsson et al., 2015; Ritz et al., 2021), which is confirmed in the models with ETAS-
484 f outperforming all other models. The area also sees drastically varying rates of seismic-
485 ity with three high-intensity events in October 2020, November 2020, and January 2021,
486 when seismicity rates surpass 75 events per week. In this later part of the forecasting
487 period, all advanced ETAS models see a stark change in their predictive capabilities and
488 start performing better than ETAS-0 (Figure 9 top left panel). These periods of high

seismic intensity are the ones that see the Seismogenic Index's performance plummet (Figure 9 is cut-off at -600, but by the end of the forecasting period, the Seismogenic Index's log-likelihood accumulates down to -4100).

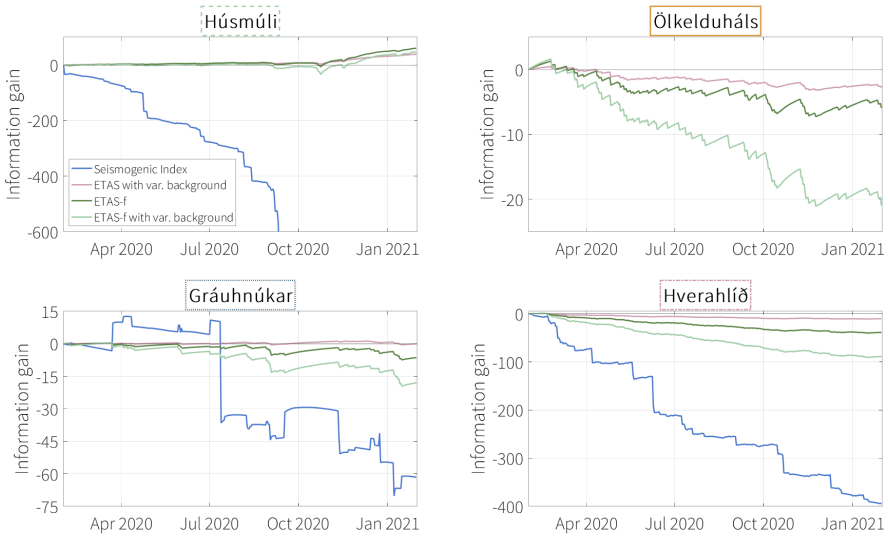

Figure 9. Information gain by subregion for the Seismogenic index and the different ETAS models calculated relative to ETAS-0.

Figure 7 shows the Seismogenic Index as the best performing model for the first half of the year of forecasting. However, the only areas where this is highlighted in Figure 9 is Gráuhnúkar, where the performance is marginally better than the ETAS models. This means that outside of our areas of interest (and in the cells where there is injections and/or production), the Seismogenic Index performs quite well compared to the ETAS models.

5.3 Adaptability to rapid seismicity rate changes

We now focus on the Húsmúli reinjection area that sees semi-periodic bursts of seismic activity which do not seem to be linked to changes in the injection rate, temperature or well-split (Figure 10-a). The origin of these high-intensity periods of seismicity in unclear, they could be induced, linked to the volcanic activity of the region or to the rift (personal communication S. Krisjánsdóttir). In this section, we investigate how fast models are able to adapt to the new baseline seismicity during these high-intensity events.

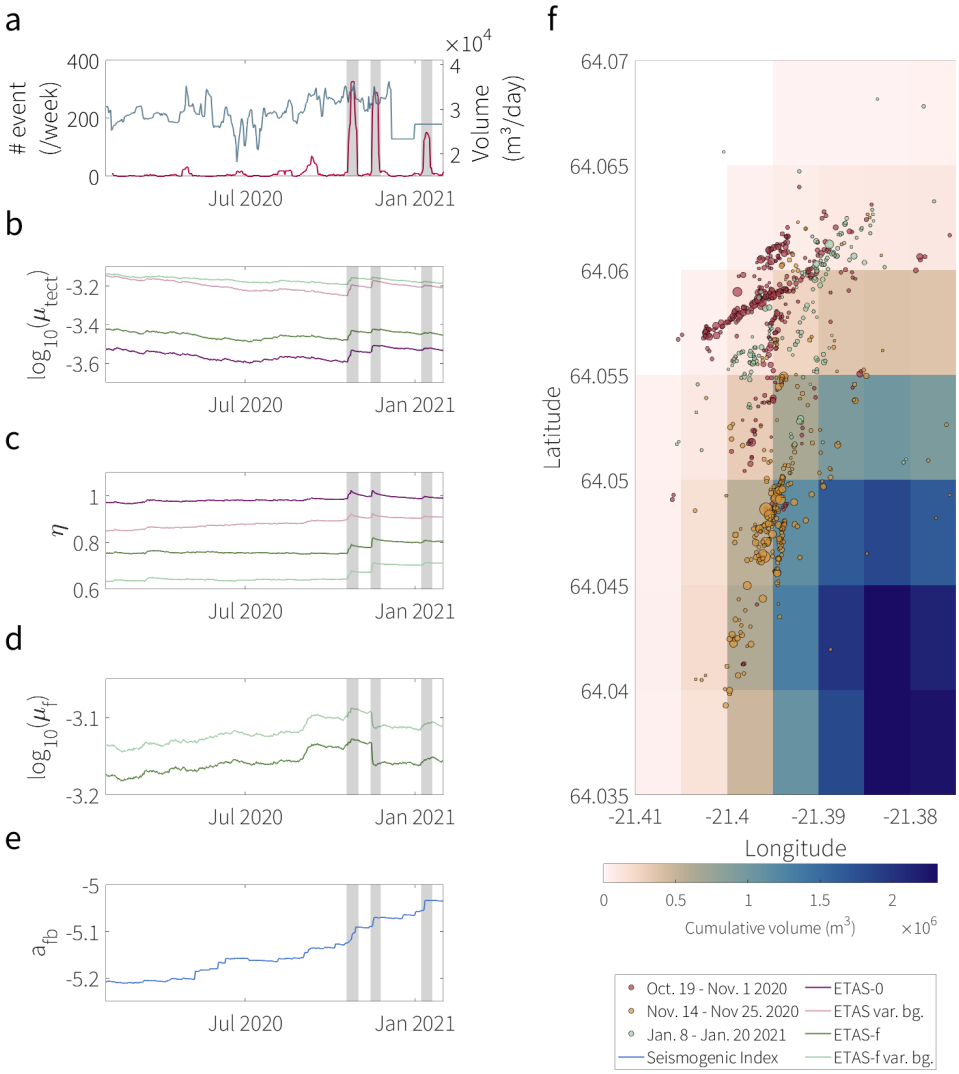

Figure 10. a) Weekly number of events recorded in Húsmúli (moving average with 1 day increment) and injection rate in the area. b-d) Evolution of the ETAS models parameters. e) Seismogenic index parameter evolution. The grey areas highlight the high-intensity periods. f) Spatial distribution of the seismicity during the high-intensity periods overlaid on the cumulative volume map.

ETAS parameters interpretation The branching ratio η represents the share of events categorised as triggered aftershocks. Shifting from ETAS-0 to a varying background rate leads to more events being classified as background, thus the lower branching ratio (Figure 10-c; Mizrahi et al. (2023)). Similarly, the ETAS-f model allows for more events to be classified into their two background categories (natural and fluid-induced), lead-

ing to an even lower base value of the branching ratio η. The effects of the free background and the additional fluid-background term add up to make ETAS-f with varying background the model with the lowest branching ratio of the class.

The tectonic background term μ_{tect} (given as number of events per km^2 per day in Figure 10) also shows this effect of increasing classification into 'background' with model complexity, with ETAS-0 at the lowest global values, ETAS-f with a significant increase in its base value due to the added fluid-background term which gives the model more flexibility to interpret events as background earthquakes, and the ETAS models with varying background at the highest base values of μ_{tect} (mean value on the active area, Figure 10-b) because they give the most flexibility to this term. If we look at the evolution of the background term in time, we notice a general decrease as the learning period length increases. Mizrahi et al. (2021b) proposed that this downwards trend denotes that longer learning periods allow models to reveal more long-term earthquake interaction and aftershock sequences, leading to more events being classified as 'triggered' as the forecasting experiments progress. This general trend of μ_{tect} is interrupted by bursts of seismic activity in the field, as highlighted by the grey areas marking the 'high-intensity periods' in Húsmúli. All ETAS models see an increase in the background rate to accommodate this new temporary baseline seismicity rate. The relaxation of μ_{tect} after the high-intensity periods is slow and seems to follow the general decreasing trend that we interpret as being due to the lengthening of the learning period.

During the high-intensity periods, the branching ratio for all models increases to accompany the increase in background seismicity rate. However, this increase is only temporary for the ETAS versions without fluid-forcing and η quickly recovers to its pre-high-intensity-period levels, whereas the ETAS-f models see a much slower recovery of η with a permanent change in the parameter resulting from the high-intensity period. These shifts in μ_{tect} and η suggest that all ETAS models accommodate the high-intensity periods by producing more background events that are also produce more aftershocks.

For the ETAS-f class, the fluid-background term μ_f (also given as number of events per km^2 per day in Figure 10) combines the scaling factor ι (Equation 12) with cumulative compound volume. While ι defines the seismicity induced by a unit volume, μ_f gives the rate of fluid induced events given the compound volume in the forecasting period. The free background version of ETAS-f shows higher base values of the fluid-background

term, mirroring the higher values of μ_{tect}. The evolution of μ_f shows a non-systematic behaviour (Figure 10-d). The first and third high-intensity periods show an increase in the productivity of fluid driven events, which is what we expect ETAS-f models to do to adapt to increasing seismicity rates in an area with active injection and/or production. However, the second high-intensity period shows a sharp drop of μ_f, maybe suggesting that ETAS-f models try to explain this change in the seismicity with tectonic events. When looking at the high-intensity periods on the map (Figure 10-f), the first and third events cluster to the north where less fluids are distributed while the second high-intensity period clusters on the edge of the most heavy reinjection region, closer to the injection wells. This might suggest that peripheral regions can be more sensitive to fluid during certain periods, while the center of the area has so much fluid injected/extracted continuously that ETAS-f models can't explain a sudden increase of seismicity with a change of productivity of a unit of fluid, thus a drop in μ_f down to its base value at the start of the second high-intensity period.

In the Ölkelduháls area the split background terms and set-up with the entire region used for training lead to the background terms in the case of ETAS-f being larger than for the standard ETAS. This calibration on the entire region also leads the triggering kernels to be different for ETAS-0 and ETAS-f, which drives the models to assign events as 'background', 'triggered' or 'induced' differently. Thus, even in areas without fluids, ETAS-f provides a different forecast than ETAS-0. If the ETAS-f model had been trained only in Ölkelduháls, ETAS-0 and ETAS-f would yield the exact same forecast.

Supplementary Figure S2 shows the evolution of the parameters describing the aftershock distribution in time and space for all models of the ETAS class.

Seismogenic Index parameter evolution The average value of the productivity parameter a_{fb} increases in time to accommodate the change in seismicity rate (Figure 10-e). Figure 11 shows a break down of the change of a_{fb} in time in the three subregions where fluids are injected and/or produced. The activation feedback is much higher in the reinjection regions and Hverahlíð production area than the average shown in Figure 10-e, highlighting the regions as seats of seismicity. The value of a_{fb} is quite stable in Hverahlíð, where the production rate and seismicity rate are relatively constant during the forecasting experiment (Figures 4 and 8). On the contrary, in the injection regions of Gráuhnúkar and Húsmúli, where both the seismicity and injection rates have

a more jagged behaviour, the value of a_{fb} sees sharp increases to try to accommodate the changing rate of seismicity. The case of Gráuhnúkar in particular shows that these 'spikes' in a_{fb} are followed by a slow healing phase during which the parameter is gradually lowered.

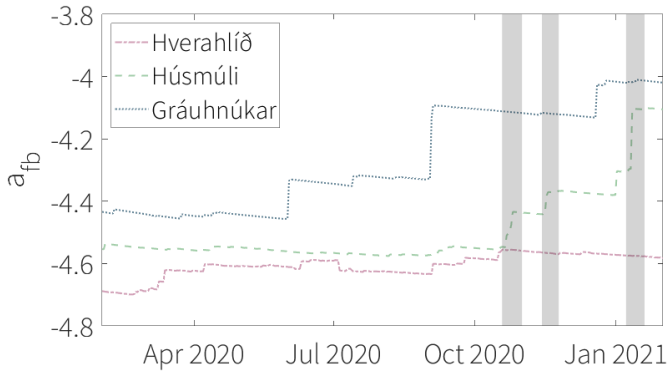

Figure 11. Evolution of the activation feedback in time during the forecasting experiment by subregion.

If we compare the fluid scaling factor ι for ETAS-f models and the Seismogenic Index's a_{fb} as analogous 'seismic productivity per unit volume' terms, we notice a similar relative increase in the first half of the forecasting period. However, the fluid productivity terms show different reactions to the high-intensity periods. The Seismogenic Index model only has this parameter to adapt to the fast changes in the seismicity rate, while ETAS-f models are able to explain the shift in seismicity rate with other parameters for example assigned them as background or naturally triggered events.

6 Discussion

All the models used seem well suited to modelling seismicity in the Hengill geothermal field, although they show their respective limitations in specific subregions or following unexpected and abrupt changes in the seismicity rate.

However, the set-up of our pseudo-forecasting experiment also reveals some of its limits. First of all, the modelled period needs to match the length of operations in the field to provide a complete picture of the processes. As we saw in the Gráuhnúkar area, a 14 months training period on a reinjection in operation since 2006 with stable seismicity and injection rates can lead to a misattribution of the induced seismicity as background

by ETAS-f models. The choice of the learning and forecasting periods was dictated by the high quality seismic catalogue, however, it would be interesting to run a much longer term experiment that encompasses pre-reinjection times to see if ETAS-f models pick up on the onset of the injection-induced seismicity.

Following up on this point, the discrimination between induced and natural seismicity that ETAS-f models allow has not been fully explored. In particular, one could look at the attribution of aftershock sequences to induced or natural events. So far, the use of both ETAS and Seismogenic Index models only tell us broad information, for example, the case of Ölkelduháls, which must be a natural sequence (or induced by naturally occurring fluids) as no injection or production is taking place in the vicinity.

Another important aspect of induced seismicity mitigation methods relies on linking modelling results to hazard and risk calculations (Broccardo et al., 2019; Schultz et al., 2021, 2022). In this work, we stopped on the level of forecasting seismicity rates and did not venture further, however, we do plan to expand to hazard and risk in future work.

6.1 Future improvements to the models

Seismogenic Index model In this study, we used the most simple implementation of the Seismogenic Index possible, and could likely improve its performance in two ways. First, by improving the way how to account for the uncertainties of the model parameters replacing the Poissonian assumption by a method sampling from the parameter space around the optimised model parameters and defining a confidence interval around them (Rinaldi & Passarelli, 2021). Furthermore, as suggested by Broccardo et al. (2017), a Bayesian optimisation approach using prior-distributions of the model parameters gathered from past induced seismicity cases in geothermal exploration sites, would be advantageous for two reasons: First, a model using the Bayesian theorem would automatically give a pseudo-poissonian probabilistic output in form of a posterior distribution in terms of e.g. seismicity rate. Secondly, such a model would be able to give a forecast also for cells that do not present an event during the training phase, contrary to the currently implemented version. Secondly, the distribution of volumes in space can be widely improved, taking into account the field anisotropy driven by faults and fractures, as well as well directionality. Supplementary Figure S3 shows an example of circular versus elliptical Gaussian distribution to account for well direction and faults in the Húsmúli region. These results

show that the distribution of volumes improves the performance of the Seismogenic Index by about 5% by accounting for a first order of subsurface anisotropy.

ETAS models In this work, we tested different variations of ETAS, from the standard implementation to a version with fluid-forcing. However, this is only the beginning as many more things could be implemented into ETAS to increase its predictive skill in complex systems. For example, we saw that the ETAS-f class seems promising for reinjection regions but performs poorly in production regions. Production induced seismicity is known to be linked to poroelastic stress changes (Segall, 1989; Zbinden et al., 2017). We want to introduce a proxy for poroelasticiy in ETAS to account better for this phenomenon. This ETAS-poroelasticity would need to be tested separately on production regions, to emancipate ourselves from the noise of reinjection-induced seismicity and natural seismicity present in the Hengill field ((Goebel et al., 2017; Segall & Lu, 2015)).

In our current implementation, we distributed the volumes without accounting for the faults and geological unit adding anisotropy to the underground. We however have hydro-geological models at our disposal both for the Húsmúli reinjection area and Hengill-wide field (TOUGH2 models provided by Reykjavik Energy; Ritz et al. (2021)). These models could be coupled to ETAS (and to the Seismogenic Index model) into a hybrid model to give ETAS and the Seismogenic Index model a more realistic representation of the flow rate and volume distribution in the field. Such models with high-resolution local information on the fluid flow could help support operators in the well-sitting process. Indeed, the combination of a calibrated fluid- and heat-flow model with seismicity forecasting models provide a rare insight to decide on the development of production and injection areas while combining productivity information and a proxy for the seismic risk.

Other models Beyond ETAS and Seismogenic Index models, we could test other statistical models in a similar pseudo-forecasting framework. For example, we could design an extremely simple model like "the rate that one will observe in the forecast is the same as the average in the last X weeks", and use it as a reference model instead of comparing all models to ETAS-0.

Purely statistical description of earthquakes in time and space are however limited as they do not account for the physical mechanisms behind induced seismicity. These mechanisms include static and dynamic stress transfer, the frictional properties of faults,

as well as changes in pore pressure which are fundamental to explain induced events. Physics-based models able to describe aftershock triggering (e.g. Coulomb models; King et al. (1994); Catalli et al. (2016)) could be useful in complex contexts like Hengill. Physics-based model range from the simpler with analytical solutions for pore-pressure to more advanced ones like rate-and-state or models incorporating elements of poroelasticity. This last point would be interesting to compare in the production area of Hverahlíð where we saw that using the produced volume as a proxy is not very successful. Hardebeck (2021) notes a general under-performance of Coulomb-Rate-and-State models relative to ETAS models, but argues that incorporating heterogeneities in background conditions into physical forecasting models may be key in improving their performance. This conclusion is supported by Mancini et al. (2019), which however argues that stress-based models which consider secondary triggering mechanisms (stress changes, earthquake interactions) can preform similarly to ETAS in complex sequences.

7 Conclusion

The complexity of the seismicity in the Hengill geothermal field, with natural and induced events, as well as sudden periods of high-intensity activity, makes it an interesting but challenging testing ground for forecasting models. As we've seen, the Seismogenic Index and ETAS models are well suited to forecasting the seismicity in the field and its different subregions, although the former can only produce a forecast in active injection and/or production regions. In such a complex geothermal field, the Seismogenic Index model performs similarly or better than ETAS models as long as the rate of seismicity remains relatively stable. As soon as an abrupt change in the seismicity rate occurs, the Seismogenic Index model perform significantly worse than any ETAS model. One major advantage of ETAS models lay in their ability to forecast natural seismicity, which allows them to fit data even in areas where no fluids are injected (as seen in Ölkelduháls).

Although there are still routes to explore to improve individual models, as highlighted in the Discussion section, the respective strengths of the models could be harvested by using an ensemble modelling framework. The concept to combine different models to obtain more robust forecasts and limit the individual model's biases, has been widely tested in recent years with all sorts of forecasting models (Marzocchi et al., 2012; Llenos & Michael, 2019; Bayona et al., 2021; Király-Proag et al., 2018; Dempsey & Suckale, 2017;

Mizrahi et al., 2023). Such an approach with ETAS and Seismogenic Index-type models could prove useful as near-real-time tools in areas experiencing induced seismicity like Oklahoma or near the Groningen gas field in the Netherlands.

Hydraulic data is often difficult to stream in real time and might not be available with fine enough granularity to be useful for forecasting exercises. ETAS-0 does not require this input of fluids to yield forecasts. In the event that injection and/or production rates are available in real-time, ETAS with fluid forcing performs slightly better than standard ETAS and could easily be run in parallel to a Seismogenic Index model in an operational forecasting tool.

Data Availability Statement

Seismic catalogue: Grigoli et al. (2022)

Seismic network: 2C network, Swiss Seismological Service at ETH Zurich (2018)

Hydraulic data: `https://doi.org/10.5281/zenodo.7795612`

Author statement

V. A. Ritz: Conceptualization, Methodology, Software, Formal Analysis, Data Curation, Visualization

L. Mizrahi: Methodology, Software, Formal Analysis, Visualization

V. Clasen Repollés: Software, Formal Analysis

A. P. Rinaldi: Conceptualization, Methodology, Validation, Supervision

V. Hjörleifsdóttir: Data Curation

S. Wiemer: Supervision, Funding Acquisition

All authors participated in the writing, review and editing of the manuscript.

Acknowledgments

Shyam Nandan is gratefully acknowledged for his support and discussions on the ETAS-class models.

The authors thank Pilar Sánchez-Pastor for the valuable discussions about the Hengill field and its geophysical characterisation.

Thomas Ratouis is gratefully acknowledged for providing the hydraulic data on behalf of Reykjavik Energy. This project has been subsidised through the ERANET Co-

fund GEOTHERMICA (Project no. 731117), from the European Commission and the SFOE under contract number SI/501721.

This work forms part of the DEEP project (`http://deepgeothermal.org`) funded through the ERANET Cofund GEOTHERMICA (Project No. 200320-4001) from the European Commission. The DEEP project benefits from an exploration subsidy of the Swiss federal office of energy for the EGS geothermal project in Haute-Sorne, canton of Jura (contract number MF-021-GEO-ERK), which is gratefully acknowledged.

Real-time Earthquake Risk Reduction for a Resilient Europe 'RISE' project has received funding from the European Union's Horizon 2020 research and innovation programme under grant agreement No 821115.

References

Ágústsson, K., Kristjánsdóttir, S., Flóvenz, O. G., Guðmundsson, O., Flóvenz, G., & Guðmundsson, (2015). Induced Seismic Activity during Drilling of Injection Wells at the Hellisheiði Power Plant, SW Iceland. In *World geothermal congress 2015.*

Axelsson, G. (2012). Role and Management of Geothermal Reinjection. *"Short Course on Geothermal Development and Geothermal Wells", organized by UNU-GTP and LaGeo, in Santa Tecla, El Salvador, March 11-17, 2012.*, 1–21.

Bachmann, C. E., Wiemer, S., Woessner, J., & Hainzl, S. (2011). Statistical analysis of the induced Basel 2006 earthquake sequence: introducing a probability-based monitoring approach for Enhanced Geothermal Systems. *Geophysical Journal International*, *186*(2), 793–807. doi: 10.1111/j.1365-246X.2011.05068.x

Bayona, J. A., Savran, W., Strader, A., Hainzl, S., Cotton, F., & Schorlemmer, D. (2021). Two global ensemble seismicity models obtained from the combination of interseismic strain measurements and earthquake-catalogue information. *Geophysical Journal International*, *224*, 1945–1955. doi: 10.1093/gji/ggaa554

Blanck, H., Vogfjörd, K., Geirsson, H., & Hjörleifsdóttir, V. (2021). Using Seismicity to Map Fractures in Hengill , SW-Iceland. *Proceedings World Geothermal Congress 2020+1*(October), 1–8.

Bourne, S. J., & Oates, S. J. (2017). Development of statistical geomechanical

models for forecasting seismicity induced by gas production from the Groningen field. *Geologie en Mijnbouw/Netherlands Journal of Geosciences*, *96*(5), s175-s182. doi: 10.1017/njg.2017.35

Broccardo, M., Mignan, A., Grigoli, F., Karvounis, D., Rinaldi, A. P., Danciu, L., ... Wiemer, S. (2019). Induced seismicity risk analysis of the hydraulic stimulation of a geothermal well on Geldinganes, Iceland. *Natural Hazards and Earth System Sciences Discussions*(November), 1–39. doi: 10.5194/nhess-2019-331

Broccardo, M., Mignan, A., Wiemer, S., Stojadinovic, B., & Giardini, D. (2017). Hierarchical Bayesian Modeling of Fluid-Induced Seismicity. *Geophysical Research Letters*, *44*(22), 311–357. doi: 10.1002/2017GL075251

Catalli, F., Rinaldi, A. P., Gischig, V. S., Nespoli, M., & Wiemer, S. (2016). The importance of earthquake interactions for injection-induced seismicity: Retrospective modeling of the Basel Enhanced Geothermal System. *Geophysical Research Letters*, *43*(10), 4992–4999. doi: 10.1002/2016GL068932

Clauset, A., Shalizi, C. R., & Newman, M. E. (2009). Power-law distributions in empirical data. *SIAM Review*, *51*(4), 661–703. doi: 10.1137/070710111

Decriem, J., Árnadóttir, T., Hooper, A., Geirsson, H., Sigmundsson, F., Keiding, M., ... Bennett, R. A. (2010). The 2008 May 29 earthquake doublet in SW Iceland. *Geophysical Journal International*, *181*(2), 1128–1146. doi: 10.1111/j.1365-246X.2010.04565.x

Dempsey, D., & Suckale, J. (2017). Physics-based forecasting of induced seismicity at Groningen gas field, the Netherlands. *Geophysical Research Letters*, *44*(15), 7773–7782. doi: 10.1002/2017GL073878

Dinske, C., & Shapiro, S. A. (2013). Seismotectonic state of reservoirs inferred from magnitude distributions of fluid-induced seismicity. *Journal of seismology*, *17*(1), 13–25.

Ducrocq, C., Geirsson, H., Árnadóttir, T., Juncu, D., Drouin, V., Gunnarsson, G., ... Blanck, H. (2021). Inflation-Deflation Episodes in the Hengill and Hrómundartindur Volcanic Complexes, SW Iceland. *Frontiers in Earth Science*, *9*(October), 1–18. doi: 10.3389/feart.2021.725109

Flóvenz, G., Ágústsson, K., Guðnason, , Kristjánsdóttir, S., Árni Guðnason, E., & Kristjánsdóttir, S. (2015). Reinjection and Induced Seismicity in Geothermal Fields in Iceland. *Proceedings World Geothermal Congress*(April), 1–15.

Foulger, G. R., & Toomey, D. R. (1989). Structure and evolution of the Hengill-Grensdalur volcanic complex, Iceland: geology, geophysics, and seismic tomography. *Journal of Geophysical Research*, *94*(B12). doi: 10.1029/jb094ib12p17511

Franzson, H., Guðfinnsson, G. H., Helgadóttir, H. M., & Frolova, J. (2010). Porosity, density and chemical composition relationships in altered icelandic hyaloclastites. *Water-Rock Interaction*(Frolova 2005), 199–202.

Franzson, H., Kristjánsson, B. R., Gunnarsson, G., Björnsson, G., Hjartarson, A., Steingrímssom, B., ... Gíslason, G. (2005). The Hengill-Hellisheiði geothermal field. Development of a conceptual geothermal model. In *Proceedings world geothermal congress 2005* (pp. 24–29).

Goebel, T. H. W., Kwiatek, G., Becker, T. W., Brodsky, E. E., & Dresen, G. (2017). What allows seismic events to grow big?: Insights from b-value and fault roughness analysis in laboratory stick-slip experiments. *Geology*, *45*(9), 815–818. doi: 10.1130/G39147.1

Grigoli, F., Cesca, S., Priolo, E., Rinaldi, A. P., Clinton, J. F., Stabile, T. A., ... Dahm, T. (2017). Current challenges in monitoring, discrimination, and management of induced seismicity related to underground industrial activities: A European perspective. *Reviews of Geophysics*, *55*(2), 310–340. doi: 10.1002/2016RG000542

Grigoli, F., Clinton, J. F., Diehl, T., Kaestli, P., Scarabello, L., Agustsdottir, T., ... Wiemer, S. (2022). Monitoring microseismicity of the Hengill Geothermal Field in Iceland. *Scientific Data*, 1–11. doi: 10.1038/s41597-022-01339-w

Gunnarsson, G. (2013). Temperature dependent injectivity and induced seismicity - Managing reinjection in the Hellisheidi Field, SW-Iceland. *Transactions - Geothermal Resources Council*, *37*(PART 2), 1019–1025.

Gunnarsson, G., Arnaldsson, A., & Oddsdóttir, A. L. (2011). Model Simulations of the Hengill Area, Southwestern Iceland. *Transport in Porous Media*, *90*(1), 3–22. doi: 10.1007/s11242-010-9629-1

Gunnarsson, G., Kristjánsson, B. R., Gunnarsson, I., & Júlíusson, B. M. (2015). Reinjection into a Fractured Reservoir – Induced Seismicity and Other Challenges in Operating Reinjection Wells in the Hellisheiði Field , SW-Iceland. In *Proceedings world geothermal congress 2015* (pp. 19–25).

Gunnlaugsson, E., & Ívarsson, G. (2010). Direct Use of Geothermal Water for District Heating in Reykjavík and Other Towns and Communities in SW-Iceland. In *Proceedings world geothermal congress* (pp. 25–29).

Hardarson, B. S., Einarsson, G. M., Kristjánsson, B. R., Gunnarsson, G., & Helga, M. (2010). Geothermal Reinjection at the Hengill Triple Junction , SW Iceland. *Stanford Geothermal Conference*(April), 25–29.

Hardebeck, J. L. (2021). Spatial Clustering of Aftershocks Impacts the Performance of Physics-Based Earthquake Forecasting Models. *Journal of Geophysical Research: Solid Earth*, *126*(2), 1–16. doi: 10.1029/2020JB020824

Hersir, G. P., Arnson, K., & Steingrimsson, B. (2009). EXPLORATION AND DEVELOPMENT OF THE HENGILL GEOTHERMAL FIELD. In *Short course on surface exploration for geothermal resources* (pp. 1–12).

Hjörleifsdóttir, V., Ósk Snaebjörnsdóttir, S., Gunnarsson, G., Kristjánsson, B. R., Vogfjord, K., Jónsdóttir, K., ... Geirsson, H. (2021). Induced Earthquakes in the Hellisheiði Geothermal Field, Iceland. In *Proceedings world geothermal congress 2020+1* (pp. 1–6).

Jakobsdóttir, S. S. (2008). Seismicity in Iceland: 1994-2007. *Jökull*, *58*(58), 75–100.

Jousset, P., Haberland, C., Bauer, K., & Arnason, K. (2011). Hengill geothermal volcanic complex (Iceland) characterized by integrated geophysical observations. *Geothermics*, *40*(1), 1–24. doi: 10.1016/j.geothermics.2010.12.008

Jousset, P., Haberland, C., Bauer, K., Arnason, K., Weber, M., & Fabriol, H. (2010). Seismic Tomography and Long-Period Earthquakes Observation and Modelling at the Hengill Geothermal Volcanic Complex , Iceland. *Proceedings World Geothermal Congress 2010*(April), 25–29.

Juncu, D., Árnadóttir, T., Geirsson, H., Guðmundsson, G. B. B., Lund, B., Gunnarsson, G. I., ... Michalczewska, K. (2018). Injection-induced surface deformation and seismicity at the Hellisheidi geothermal field, Iceland. *Journal of Volcanology and Geothermal Research*, *391*. doi: 10.1016/j.jvolgeores.2018.03.019

Juncu, D., Árnadóttir, T., Hooper, A., & Gunnarsson, G. (2017). Anthropogenic and natural ground deformation in the Hengill geothermal area, Iceland. *Journal of Geophysical Research: Solid Earth*, *122*(1), 692–709. doi: 10.1002/2016JB013626

Kagan, Y. Y., & Knopoff, L. (1987). Statistical Short-Term Earthquake Prediction. *Science*, *236*(4808), 1563–1567. doi: https://doi.org/10.1126/science.236.4808.1563

King, G. C. P., Stein, R. S., & Lin, J. (1994). Static stress changes and the triggering of earthquakes. *Bulletin of the Seismological Society of America*, *84*(3), 935–953.

Király-Proag, E., Gischig, V. S., Zechar, J. D., & Wiemer, S. (2018). Multicomponent ensemble models to forecast induced seismicity. *Geophysical Journal International*, *212*(1), 476–490. doi: 10.1093/gji/ggx393

Király-Proag, E., Zechar, J. D., Gischig, V. S., Wiemer, S., Karvounis, D. C., & Doetsch, J. (2016). Validating induced seismicity forecast models—Induced Seismicity Test Bench. *Journal of Geophysical Research: Solid Earth*, *121*(8), 6009–6029. doi: 10.1002/2016JB013236

Kristjansdottir, S., Gudmundsson, O., Agustsson, K., Agustsdottir, T., Tryggvason, A., & Fehler, M. (2021). Induced Seismicity during Reinjection of Wastewater in Hellisheidi Geothermal Field, SW Iceland. In *Proceedings world geothermal congress 2020+1* (pp. 1–8).

Llenos, A. L., & Michael, A. J. (2019). Ensembles of ETAS Models Provide Optimal Operational Earthquake Forecasting During Swarms : Insights from the 2015 San Ramon , California Swarm. *Bulletin of the Seismological Society of America*, *109*(6), 2145–2158. doi: 10.1785/0120190020

Mancini, S., Segou, M., Werner, M. J., & Cattania, C. (2019). Improving Physics-Based Aftershock Forecasts During the 2016–2017 Central Italy Earthquake Cascade. *Journal of Geophysical Research: Solid Earth*, *124*(8), 8626–8643. doi: 10.1029/2019JB017874

Mancini, S., Werner, M. J., Segou, M., & Baptie, B. (2021). Probabilistic Forecasting of Hydraulic Fracturing-Induced Seismicity Using an Injection-Rate Driven ETAS Model. *Seismological Research Letters*. doi: 10.1785/0220200454

Marzocchi, W., Lombardi, A. M., & Casarotti, E. (2014). The establishment of an operational earthquake forecasting system in Italy. *Seismological Research Letters*, *85*(5), 961–969. doi: 10.1785/0220130219

Marzocchi, W., & Sandri, L. (2003). A review and new insights on the estimation of the. *Annals of Geophysics*, *46*(6), 1271–1282.

Marzocchi, W., Zechar, J. D., & Jordan, T. H. (2012). Bayesian Forecast Evaluation and Ensemble Earthquake Forecasting. *Bulletin of the Seismological Society of America*, *102*(6), 2574–2584. doi: 10.1785/0120110327

Mena, B., Wiemer, S., & Bachmann, C. (2013). Building robust models to forecast the induced seismicity related to geothermal reservoir enhancement. *Bulletin of the Seismological Society of America*, *103*(1), 383–393. doi: 10.1785/0120120102

Mignan, A. (2016). Static behaviour of induced seismicity. *Nonlinear Processes in Geophysics*, *23*(2), 107–113. doi: 10.5194/npg-23-107-2016

Mignan, A., Broccardo, M., & Wang, Z. (2021). Comprehensive Survey of Seismic Hazard at Geothermal Sites by a Meta-Analysis of the Underground Feedback Activation Parameter a fb. *Energies*, *14*(7998), 1–15. doi: https://doi.org/10.3390/en14237998

Mignan, A., Broccardo, M., Wiemer, S., & Giardini, D. (2017). Induced seismicity closed-form traffic light system for actuarial decision-making during deep fluid injections. *Scientific Reports*, *7*(1). doi: 10.1038/s41598-017-13585-9

Mignan, A., Broccardo, M., Wiemer, S., & Giardini, D. (2019). Autonomous decision-making against induced seismicity in deep fluid injections. In *Springer series in geomechanics and geoengineering* (pp. 369–376). doi: 10.1007/978-3-319-99670-7{\{}{\textbackslash}{_}{\}}46

Mizrahi, L., Nandan, S., Savran, W., Wiemer, S., & Ben-Zion, Y. (2023). Question-Driven Ensembles of Flexible ETAS Models. *Seismological Research Letters*(March). doi: 10.1785/0220220230

Mizrahi, L., Nandan, S., & Wiemer, S. (2021a). The effect of declustering on the size distribution of mainshocks. *Seismological Research Letters*, *92*(4), 2333–2342. doi: 10.1785/0220200231

Mizrahi, L., Nandan, S., & Wiemer, S. (2021b). Embracing Data Incompleteness for Better Earthquake Forecasting. *Journal of Geophysical Research: Solid Earth*, *126*(12), 1–26. doi: 10.1029/2021JB022379

Nandan, S., Kamer, Y., Ouillon, G., Hiemer, S., & Sornette, D. (2021). Global models for short-term earthquake forecasting and predictive skill assessment. *European Physical Journal: Special Topics*, *230*(1), 425–449. doi: 10.1140/epjst/e2020-000259-3

Ogata, Y. (1988). Statistical Models for Earthquake Occurrences and Residual Analysis for Point Processes. *Journal of the American Statistical Association*, *83*(401), 9–27. doi: http://dx.doi.org/10.1080/01621459.1988.10478560

Rinaldi, A. P., & Passarelli, L. (2021). *DEEP Deliverable 3.1 - Extensive comparison of existing forecasting induced seismicity models with existing datasets* (Tech. Rep.).

Ritz, V. A., Rinaldi, A. P., Karvounis, D., Castilla, R., Colas, E., Meier, P. M., ... Gunnarsson, G. (2021). Preliminary Modelling Activities for an Adaptive Traffic Light System for the Hengill Geothermal Field. *World Geothermal Congress Proceedings 2020*(October), 1–8.

Saemundsson, K. (1992). Geology of the Thingvallavatn Area. *Oikos*, *64*(1), 40–68. doi: http://www.jstor.com/stable/3545042REFERENCES

Sánchez-Pastor, P., Obermann, A., Reinsch, T., Ágústsdóttir, T., Gunnarsson, G., Tómasdóttir, S., ... Wiemer, S. (2021). Imaging high-temperature geothermal reservoirs with ambient seismic noise tomography, a case study of the Hengill geothermal field, SW Iceland. *Geothermics*, *96*(June). doi: 10.1016/j.geothermics.2021.102207

Schultz, R., Beroza, G. C., & Ellsworth, W. L. (2021). A risk-based approach for managing hydraulic fracturing–induced seismicity. *Science*, *372*(6541), 504–507. doi: 10.1126/science.abg5451

Schultz, R., Ellsworth, W. L., & Beroza, G. C. (2022). Statistical bounds on how induced seismicity stops. *Scientific Reports*, 1–11. Retrieved from `https://doi.org/10.1038/s41598-022-05216-9` doi: 10.1038/s41598-022-05216-9

Segall, P. (1989). Earthquakes triggered by fluid extraction. *Geology*, *17*(10), 942–946.

Segall, P., & Lu, S. (2015). Injection-induced seismicity: Poroelastic and earthquake nucleation effects. *Journal of Geophysical Research: Solid Earth*, *120*(7), 5082–5103. doi: 10.1002/2015JB012060

Shapiro, S. A. (2018). Seismogenic Index of Underground Fluid Injections and Productions. *Journal of Geophysical Research: Solid Earth*, *123*(9), 7983–7997. doi: 10.1029/2018JB015850

Shapiro, S. A., Dinske, C., Langenbruch, C., & Wenzel, F. (2010). Seismogenic index and magnitude probability of earthquakes induced during reservoir fluid

stimulations. *The Leading Edge*, *29*(3), 304–309. doi: 10.1190/1.3353727

Snaebjonsdottir, S. O., Tomasdóttir, S., Sigfusson, B., Aradóttir, E. S. P., Gunnarsson, G., Niemi, A., ... Franzson, H. (2018). The geology and hydrology of the CarbFix2 site, SW-Iceland. *Energy Procedia*, *146*, 146–157. doi: 10.1016/j.egypro.2018.07.019

Steigerwald, L., Einarsson, P., & Hjartardóttir, R. (2020). Fault kinematics at the Hengill Triple Junction, SW-Iceland, derived from surface fracture pattern. *Journal of Volcanology and Geothermal Research*, *391*, 106439. doi: 10.1016/j.jvolgeores.2018.08.017

Swiss Seismological Service at ETH Zurich. (2018). *COSEISMIQ - COntrol SEISmicity and Manage Induced earthQuakes.* ETH Zurich. doi: https://doi.org/10.12686/sed/networks/2c

Tomasdóttir, S. (2018). *Flow Paths in the Húsmúli Reinjection Zone , Iceland* (Unpublished doctoral dissertation). Uppsala Universitet.

Veen, A., & Schoenberg, F. P. (2008). Estimation of space-time branching process models in seismology using an EM-type algorithm. *Journal of the American Statistical Association*, *103*(482), 614–624. doi: 10.1198/016214508000000148

Verdon, J. P., & Budge, J. (2018). Examining the capability of statistical models to mitigate induced seismicity during hydraulic fracturing of shale gas reservoirs. *Bulletin of the Seismological Society of America*, *108*(2), 690–701. doi: 10.1785/0120170207

Zbinden, D., Rinaldi, A. P., Urpi, L., & Wiemer, S. (2017). On the physics-based processes behind production-induced seismicity in natural gas fields. *Journal of Geophysical Research: Solid Earth*, *122*(5), 3792–3812. doi: 10.1002/2017JB014003